Materials Research Proceedings 44 (2024) 79-89 https://doi.org/10.21741/9781644903254-9

Superplastic microstructure characteristics and unified constitutive model of TA32 titanium alloy

LIU Yang[1,2,a], WANG Chunhui[1,2,b], LI Zhiqiang[3,c], ZHANG Ning[3,d], ZHAO Bing[3,e] and SUN Chaoyang[1,2,f *]

[1]School of Mechanical Engineering, University of Science and Technology Beijing, Beijing 100083, China

[2]Beijing Key Laboratory of Lightweight Metal Forming, Beijing 100083, China

[3]AVIC Manufacturing Technology Institute, Beijing 100024, China

[a]yliu_ustb@126.com, [b]wangch@ustb.edu.cn, [c]zqlee98@126.com, [d]zn64112@163.com, [e]zhao6833@163.com, [f]suncy@ustb.edu.cn

Keywords: TA32 Titanium Alloy, Superplasticity, Deformation Characteristics, Constitutive Model

Abstract. The superplastic deformation behavior and microstructure characteristics of TA32 titanium alloy were studied at different deformation temperatures (920-960°C) and initial strain rates (1×10^{-3}-3×10^{-3} s^{-1}). A unified constitutive model was developed and coupled with internal state variables. Results show that TA32 alloy featured steady flow stress and uniform plastic deformability under the dynamic equilibrium between softening and hardening effects. Increasing temperature and strain induced α→β phase transformation and α grain growth. Dislocation accumulation and grain boundary migration formed the dynamic recovery (DRV) and dynamic recrystallization (DRX) mechanisms. Using dislocation density, the proposed unified constitutive model built a quantitative relationship between superplastic flow stress and internal state variables such as grain size, with the correlation coefficient *R*, average absolute relative error (AARE), and root mean square error (RMSE) between the predicted and experimental stress values being 0.98, 6.91%, and 1.94, respectively. The unified constitutive model could predict well the flow stress and grain size evolution of TA32 titanium alloy during superplastic deformation.

Introduction

The recently developed near-α TA32 titanium alloy exhibits a proper match of thermal strength, fracture toughness, high-temperature creep resistance, and gas corrosion resistance at 550°C. It can satisfy the demands of microstructure uniformity and performance durability at high service temperatures, making it valuable for the aerospace and automobile lightweight fields [1, 2]. In addition, the superplastic forming (SPF) process utilizes the characteristics of titanium alloy, such as low deformation resistance above 900°C and no necking, to form components with complex structure. Therefore, it is needed to explore the mechanical behaviors, microstructure evolution, and physical-based constitutive model of TA32 titanium alloy under superplastic deformation conditions.

Generally, dislocation motion is the primary driver of alloy's microstructure evolution during viscoplastic deformation. Stored energy driven DRV/DRX and grain growth controlled by grain boundary migration are also closely associated with dislocation multiplication or annihilation. Several studies have investigated the microstructure characteristics of titanium alloys during high-temperature deformation and established the microstructure-based constitutive model to describe the multiscale deformation behavior. Babu et al. [3] investigated the deformation mechanisms of TC4 titanium alloy at thermal processing conditions and established a constitutive model based on immobile dislocation density and excess vacancy concentration. Xiao et al. [4] examined the

spheroidization of α phase and DRV/DRX effects of β phase in Ti-55511 titanium alloy and established a dislocation density-based constitutive model expressing softening and work-hardening mechanisms. Bai et al. [5] developed a unified constitutive model for two-phase titanium alloys coupled with the α phase spheroidization phenomenon, taking into account the influence of adiabatic temperature change and the evolution of phase volume fraction on the plastic strain rates. Yasmeen et al. [6] investigated the evolution of grain size, dislocation density, and phase volume fraction of TA15 titanium alloy under superplastic deformation conditions and established a set of mechanism-based unified viscoplastic constitutive equations.

This paper utilizes microstructure morphology to analyze the phase distribution, grain boundary properties, and grain size evolution of TA32 alloy under superplastic deformation. Additionally, based on multiscale experimental data, a unified constitutive model of superplasticity is developed that describes macroscopic and microscopic behaviors. Ultimately, the tens of material constants coupled with each other are solved using the multi-objective optimization function. This is expected to provide theory-based guidance for SPF process for manufacturing complex components of TA32 alloy.

Experiments

Materials and methods. The experimental material is hot rolled TA32 sheet. The actual chemical composition is Ti-4.81Al-3.31Sn-2.29Zr-0.88Mo-0.50Nb-0.19Ta-0.17Si (in wt.%). The initial microstructure observed by MV6000 optical microscope (OM) is shown in Fig. 1(a). The black β phase is clustered between white α phase in the form of strips or clumps, while the equiaxed α grains have a non-uniform distribution in grain size. The tests were carried out by a LETRYDL-20T electronic universal testing machine equipped with a specialized clamp for superplastic deformation, as shown in Fig. 1(b). The sample shape and size are shown in Fig. 1(c). The tensile deformation temperatures were 920°C, 940°C, and 960°C, and the initial strain rates are 1×10^{-3} s^{-1} and 3×10^{-3} s^{-1}. The testing procedure is shown in Fig. 1(d). The EBSD observation was conducted using a JSM-7900F scanning electron microscope with a step size of 0.35 μm.

Fig. 1. As-received material and experimental methods: (a) OM image; (b) tensile testing system ; (c) sample size; (d) testing procedure.

Results. Fig. 2(a) exhibits the true stress-strain curves of TA32 alloy. At the initial stage of deformation process, dislocation multiplication and entanglement lead to a rapid increase in stress. Inevitably, the DRV and DRX accompany the deformation under high-temperature and load conditions, causing the dislocation annihilation, the plastic deformation resistance of TA32 alloy to decrease, and the degree of stress growth to decrease sharply. Even after reaching peak stress, the stress continues to decrease as strain increases. In addition, TA32 alloy's peak stress is less than 50 MPa during superplastic deformation. Notably, at 920°C and 1×10^{-3}-3×10^{-3} s^{-1}, the flow stress changes less as the strain increases. This enables TA32 alloy to form components with uniform microstructure and mechanical properties under complex stress state.

Fig. 2(b) shows the strain hardening exponent *n* of TA32 alloy at different conditions. The data shows that at 960°C and 1×10^{-3} s^{-1}, *n* values remain around 0.2. This indicates that the strain hardening effect always dominates, and the large plastic deformation process of TA32 alloy is relatively stable and may have an optimal uniform deformability (the critical strain value of geometry instability increases). The *n* values under the remaining deformation conditions decrease as strain increases, indicating the hardening effect is weakened while the softening effect is relatively enhanced and the uniform deformability decreases (the critical strain value of geometry instability decreases). In addition, for the same strain, the *n* value increases as temperature increases and strain rate decreases, causing hardening and a decrease in plastic deformability. This is due to the long high temperature, which causes excessive grain growth, grain boundary sliding to gradually reduce, and need for larger load to overcome the internal critical shear stress [7]. In particular, the curves at 920-940°C and 1×10^{-3} s^{-1} flatten out when the strain exceeds 0.7. This may be caused by the dislocation annihilation rate gradually approaching the dislocation accumulation rate, resulting in a dynamic equilibrium between the conflicting softening and hardening mechanisms.

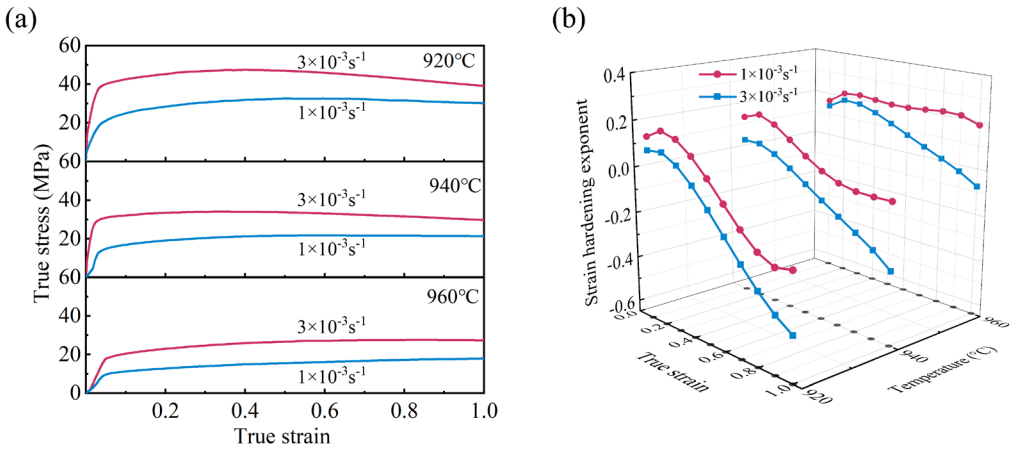

Fig. 2. (a) The true strain-stress curves and (b) strain hardening exponent.

Fig. 3 gives the α/β phase characteristics. Fig. 3(a), (b), (c), (e) and (f) demonstrate that increasing temperature and strain homogenize the two-phase microstructure and transform α to β phase. As a result, the two-phase grains become more equiaxed, and the phase boundaries are more clearly defined at 960°C/strain 1. Fig. 3(a) and (d) show that the phase volume fraction and microstructure morphology between α and β phases are similar at different strain rates. Apparently, heat and load cause small β grains to merge and grow together, while β phase gradually precipitates at α phase boundary. Eventually, the initially fragmented β phase changes to continuous or spherical. The α→β phase dynamic transformation is essentially driven by deformation storage energy and stress. The α→β diffusionless phase transformation occurs when the accumulated energy during deformation exceeds the energy barrier required for shear mode and lattice expansion. Furthermore, on one hand, high temperatures can reduce the difference in Gibbs free energy between the α and β phases and the energy required for lattice changes. On the other hand, strain concentration at the phase boundaries contributes to the change in the total free energy of the system, which promotes the phase transition through atomic diffusion. Thus, an appropriate increase in strain or temperature must result in an increase in β phase volume fraction [8].

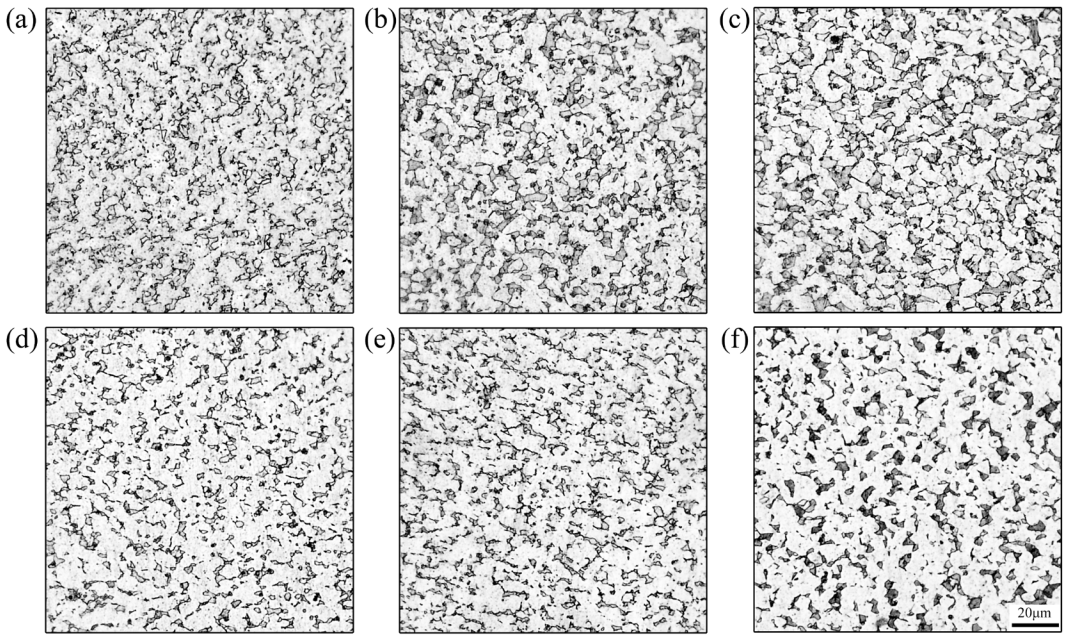

Fig. 3. The OM images of deformed microstructure: (a) 920°C/1×10^{-3} s^{-1}/strain 0.5; (b) 940°C/1×10^{-3} s^{-1}/strain 0.5; (c) 960°C/1×10^{-3} s^{-1}/strain 0.5; (d) 920°C/3×10^{-3} s^{-1}/strain 0.5; (e) 920°C/1×10^{-3} s^{-1}/strain 0.25; (f) 920°C/1×10^{-3} s^{-1}/strain 1.

Fig. 4 gives information on α grain morphology and grain boundary. A rise in temperature and strain causes the larger α_p and β grains and a more uniform α_p grain size distribution, as seen in Fig. 4(a), (b) and (c). High temperature activates grain boundary diffusion and atomic motion, causing small α grains to coalesce and grow into larger ones [9]. Additionally, LAGBs decrease with increasing temperature and strain. Generally, near LAGBs tend to have high geometrically necessary dislocation density and form channel-like structures. Dispersed intragranular dislocations gradually accumulate into dislocation walls or cells and cling more to channel-like structures, forming subgrain boundaries with higher misorientation angle, which convert LAGBs to middle-angle grain boundaries (MAGBs) (DRV effect form substructures). Moreover, under active grain boundary migration, MAGBs continue to absorb nearby free dislocations while subgrains rotate to coordinate plastic deformation. Eventually MAGBs transform into HAGBs, and the lattice distortion, non-uniform strain and high residual stress disappear, producing new equiaxed grains with uniform crystal structure (DRX effect form undistorted grains) [9, 10]. It should be noted that the increasing temperature and strain lead to the generation of finer and lamellar α_s grain (more β phase).

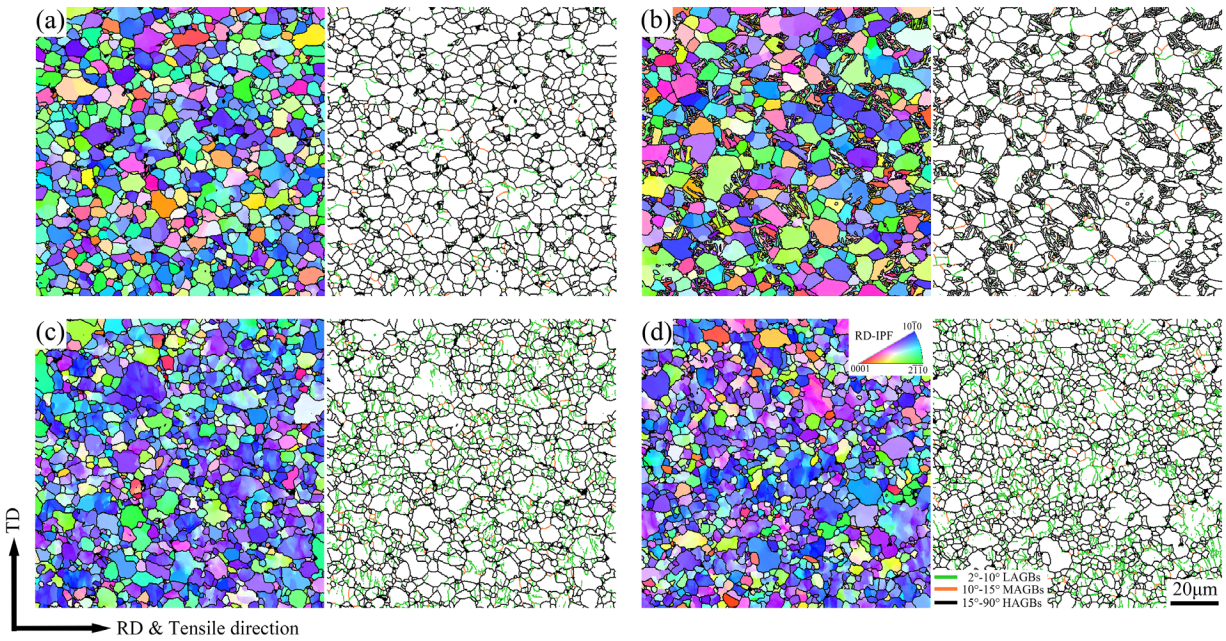

Fig. 4. The α grain morphology and grain boundary maps of deformed microstructure: (a) 920°C/1×10^{-3} s^{-1}/strain 1; (b) 960°C/1×10^{-3} s^{-1}/strain 1; (c) 920°C/1×10^{-3} s^{-1}/strain 0.25; (d) 920°C/3×10^{-3} s^{-1}/strain 0.25.

Construction of unified constitutive model

Flow rule. High rate dependency and viscoplasticity, which might be considered creep behavior, are characteristics of the superplastic deformation of titanium alloys. The basic form of the plastic stress equation combines the Rosserd equation, which describes strain hardening and strain rate hardening, and Norton's low, which describes steady state creep behavior, as follows [11]:

$$\dot{\varepsilon}_p = \left(\frac{\sigma_v}{K}\right)^n \tag{1}$$

where $\dot{\varepsilon}_p$ is plastic strain rate, σ_v is the viscoplastic stress, K is the coefficient of resistance, n is the viscosity exponent.

The true stress σ of titanium alloys during viscoplastic deformation is a linear combination of initial yield stress k, isotropic hardening stress H, and σ_v. The flow rule can be expressed as follows [12]:

$$\dot{\varepsilon}_p = \left\langle \frac{\sigma - H - k}{K} \right\rangle^n \tag{2}$$

where $\langle \square \rangle$ is the McCauley bracket, indicating that the formula in the bracket is valid only when the alloy enters the plastic deformation stage.

The H can be expressed as a function of dislocation density ρ, as follows:

$$\dot{H} = 0.5B\bar{\rho}^{-0.5}\dot{\bar{\rho}} \tag{3}$$

where B is the material constant.

The relationship between elastic strain and flow stress can be determined using Hook's law:

$$\sigma = E\left(\varepsilon_T - \varepsilon_p\right) \tag{4}$$

where E is the elastic modulus, ε_T is the total strain, ε_p is the plastic strain.

Modeling of dislocation density. The Kocks-Mecking (KM) dislocation evolution model, based on Roberts model, is applied to light alloys with an average grain size within 10 μm. The KM model considers the linear relationship between the dislocation accumulation during strain hardening and the dislocation annihilation facilitated by DRV. This can be expressed as follows:

$$\frac{d\rho}{d\varepsilon_p} = K_1\sqrt{\rho} - K_2\rho \tag{5}$$

where K_1 and K_2 are the material constants.

The normalized dislocation density evolution is expressed by considering the high-temperature deformation mechanism together as follows [13]:

$$\dot{\overline{\rho}} = A\left(1-\overline{\rho}\right)\left|\dot{\varepsilon}_p\right| - C\overline{\rho}^{n_2} \tag{6}$$

where $\overline{\rho}$ is the normalized dislocation density formulated as $\overline{\rho} = 1-\rho_0/\rho$, ρ_0 is the initial dislocation density, ρ is the dislocation density at deformation, A, n_2, and C are the material constants. The normalized dislocation density is utilized to limit the dislocation density between 0 and 1, in order to accurately describe the dislocation density evolution in the constitutive model [14, 15].

Modeling of dynamic recrystallization. The equation for the volume fraction of dynamic recrystallization controlled by dislocation and strain is as follows [16]:

$$\dot{S} = \frac{q_1\left[x\overline{\rho} - \overline{\rho}_c\left(1-S\right)\right]\left(1-S\right)^{q_2}\dot{\varepsilon}_p^{\,q_3}}{d} \tag{7}$$

where $\overline{\rho}_c$ is the critial dislocation density for dynamic recrystallization to occur and can be formulated as $\overline{\rho}_c = q_4\dot{\varepsilon}_p^{\,q_5}$ [17], d is the average grain size, q_1, q_2, q_3, q_4 and q_5 are the material constants.

The evolution rate of dynamic recrystallized onset parameter x is expressed as follows:

$$\dot{x} = q_6\left(1-x\right)\overline{\rho} \tag{8}$$

where q_6 is the material constant.

The impact of dynamic recrystallization on dislocation density must be considered as follows [11]:

$$\dot{\overline{\rho}} = A\left(1-\overline{\rho}\right)\left|\dot{\varepsilon}_p\right| - C_1\overline{\rho}^{n_2} - \left(\frac{C_2\overline{\rho}}{1-S}\right)\dot{S} \tag{9}$$

where C_2 is the material constant.

Modeling of grain size. During the high-tempertaure deformation of alloys, the grains undergo a dynamic growth and refinement process. Considering the dynamic and static grain growth as well as recrystallization assist grain refinement, the rate of grain size evolution can be expressed as follows [18, 19]:

$$\dot{d} = w_1 d^{-\gamma_1} + w_2 \dot{\varepsilon}_p d^{-\gamma_2} - w_3 \dot{S}^{\gamma_3} d^{\gamma_4} \tag{10}$$

where w_1, w_2, w_3, γ_1, γ_2, γ_3 and γ_4 are the material constants.

When considering how grain size affects flow stress, it is important to modify the plastic strain rate as follows:

$$\dot{\varepsilon}_p = \left\langle \frac{\sigma - H - k}{K} \right\rangle^{n_1} \left(\overline{d}\right)^{-u} \tag{11}$$

where u is the material constant, $\overline{d}$ is the normalized grain size formulated as $\overline{d} = d/d_i$, d and d_i are the average grain size of initial and deformed material, respectively.

Determination of material constants. In the unified constitutive model presented above, A, u, n_2, γ_2, γ_3 and γ_4 are the temperature-independent material constants. The temperature-dependent material constants are shown in Table 1. k_0, K_0, n_0, B_0, C_{10}, C_{20}, w_{10}, w_{20}, w_{30}, γ_0, q_{10}, q_{20}, q_{30}, q_{40}, q_{50}, q_{60} and E_0 are material constants. Q_k, Q_K, Q_n, Q_B, Q_{C1}, Q_{C2}, Q_{w1}, Q_{w2}, Q_{w3}, Q_γ, Q_{q1}, Q_{q2}, Q_{q3}, Q_{q4}, Q_{q5}, Q_{q6} and Q_E are activation energies linked to the temperature-dependent parameters. R is the gas constant (8.314 J mol^{-1} K^{-1}).

Table 1. The temperature-dependent parameters and their corresponding formulation.

$k = k_0 \exp\left(Q_k/RT\right)$	$w_1 = w_{10} \exp\left(Q_{w1}/RT\right)$	$q_3 = q_{30} \exp\left(Q_{q3}/RT\right)$
$K = K_0 \exp\left(Q_K/RT\right)$	$w_2 = w_{20} \exp\left(-Q_{w2}/RT\right)$	$q_4 = q_{40} \exp\left(Q_{q4}/RT\right)$
$n_1 = n_0 \exp\left(Q_n/RT\right)$	$w_3 = w_{30} \exp\left(-Q_{w3}/RT\right)$	$q_5 = q_{50} \exp\left(-Q_{q5}/RT\right)$
$B = B_0 \exp\left(Q_B/RT\right)$	$\gamma_1 = \gamma_0 \exp\left(Q_\gamma/RT\right)$	$q_6 = q_{60} \exp\left(-Q_{q6}/RT\right)$
$C_1 = C_{10} \exp\left(-Q_{C1}/RT\right)$	$q_1 = q_{10} \exp\left(-Q_{q1}/RT\right)$	$E = E_0 \exp\left(Q_E/RT\right)$
$C_2 = C_{20} \exp\left(-Q_{C2}/RT\right)$	$q_2 = q_{20} \exp\left(Q_{q2}/RT\right)$	

The material constants are searched and optimized using the genetic algorithm (GA) toolbox in Matlab software. Firstly, the computational program for unified constitutive model was programmed using the forward Euler method and iterative approach. Where Eq. 12 shows the computational and iterative procedure for each physical variable formulated by forward Euler method. The computational program was then used to program the custom function required for the GA toolbox to function properly. Finally, the GA's objective function was defined as the residual error between the predicted and experimental stress and grain size values. The global objective function is the sum of various objective functions.

$$\begin{cases} \varepsilon_{i+1}^{p} = \varepsilon_{i}^{p} + \dot{\varepsilon}_{i}^{p}\Delta t \\ \varepsilon_{i+1}^{t} = \varepsilon_{i}^{t} + \dot{\varepsilon}_{i}^{t}\Delta t \\ K_{1,i+1} = K_{1,i} + \dot{K}_{1,i}\Delta t \\ K_{2,i+1} = K_{2,i} + \dot{K}_{2,i}\Delta t \\ \cdots \\ K_{i+1} = K_{1,i+1} + K_{2,i+1} + \ldots \\ \sigma_{i+1} = E\left(\varepsilon_{i+1}^{t} - \varepsilon_{i+1}^{p}\right) \\ \sigma_{i+1} = \sigma_{i} + \Delta t \end{cases} \tag{12}$$

where K is the internal state variable, i is the iteration counter, $i = 1, 2, 3, ..., n$.

To further simplify the GA's calculation process, the custom function is modified to adapt to different deformation conditions. Then, the temperature-independent material constants are fixed, and the remaining material constants are determined using linear fitting to account for the effect of temperature. Ultimately, the optimal material constants are computed, searched for, and verified repeatedly using the GA toolbox in Matlab.

Verification of unified constitutive model

Fig. 5(a), (b) and c show the comparison between predicted stress of unified constitutive model and experimental results. The predicted values generally fit experimental values well. However, the prediction accuracy decreases in the low strains (0.05~0.4) as the temperature increases. Generally, the alloy's constitutive model often has limitations in the predicted curves under various deformation conditions that follow similar trends. Additionally, material constants solved under one condition may limit the model's accuracy under other deformation conditions. For example, the predicted curves in Fig. 5(c) resemble those in Fig. 5(b). Fig. 5(d) shows the correlation between predicted and experimental stress values. Table 2 presents the errors between predicted and experimental stress values. The correlation coefficient R, AARE and RMSE between the predicted and experimental stress values are 0.98, 6.91% and 1.94, respectively. The correlation between predicted and experimental values was strong. Under different deformation conditions, the maximum values of AARE and RMSE are 13.38% and 2.25, respectively, while the minimum values of AARE and RMSE are 2.90% and 1.55, respectively. These results suggest that the unified constitutive model has high prediction accuracy and can effectively describe the mechanic behaviors of TA32 alloy under superplastic deformation conditions.

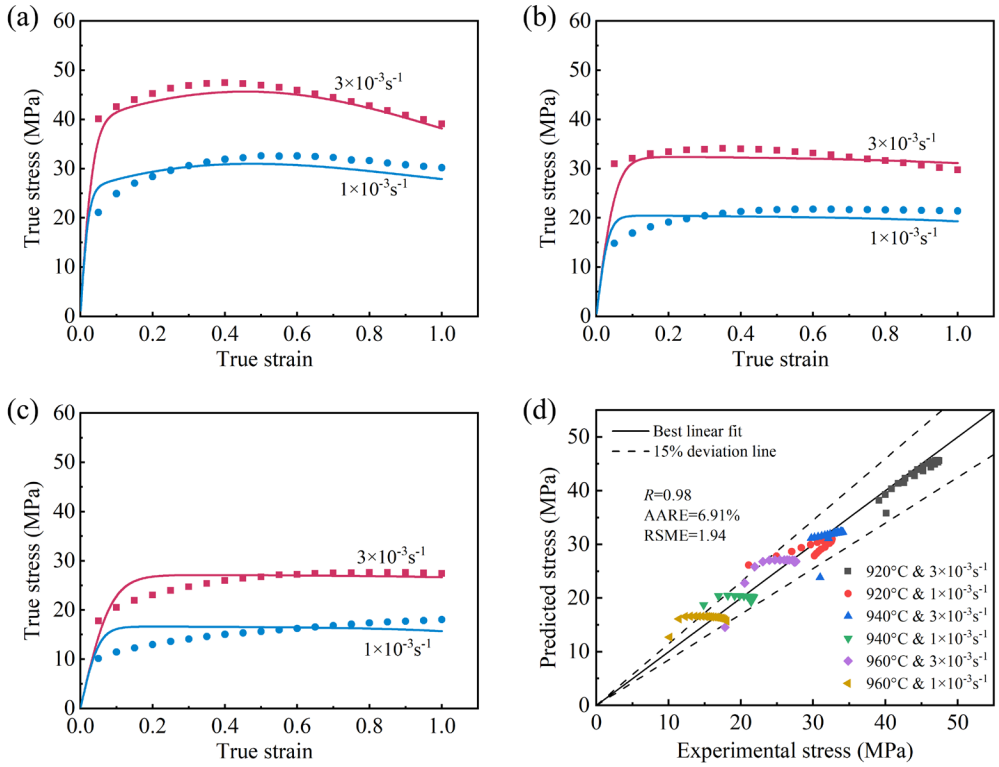

Fig. 5. Comparison between predicted stress values (curves) of constitutive model and experimental results (points): (a) 920°C, (b) 940°C and (c) 960°C; (d) correlation between predicted and experimental values

Table 2. Errors between predicted stress of constitutive model and experimental results at different deformation conditions.

	920°C and 1×10^{-3} s^{-1}	920°C and 3×10^{-3} s^{-1}	940°C and 1×10^{-3} s^{-1}	940°C and 3×10^{-3} s^{-1}	960°C and 1×10^{-3} s^{-1}	960°C and 3×10^{-3} s^{-1}
AARE	6.23%	2.90%	8.64%	4.21%	13.38%	6.07%
RMSE	2.05	1.55	1.90	1.96	2.25	1.86

Fig. 6(a) shows the comparison between predicted grain sizes of unified constitutive model and experimental results. The thermal effect causes an increase in grain size, while the dynamic recrystallization leads to a smaller grain size. So, the grain size changes dynamically during superplastic deformation. The average grain size of TA32 alloy decreases with increasing strain. On one hand, the more significant DRX effect generates finer grains. On the other hand, the water quenching following superplastic deformation of near-α titanium alloy induces the transformation of large β grains into lamellar and fine α_s grains. Fig. 6(b) illustrates the correlation between predicted and experimental normalized grain sizes, reflecting model's ability to predict internal state variable. The correlation coefficient *R*, AARE and RMSE between the predicted and experimental normalized grain size are 0.92, 4.44% and 0.051, respectively. The degree of dispersion is slightly high compared to stress. In sum, the unified constitutive model presented in this paper also has excellent accuracy in predicting internal state variable.

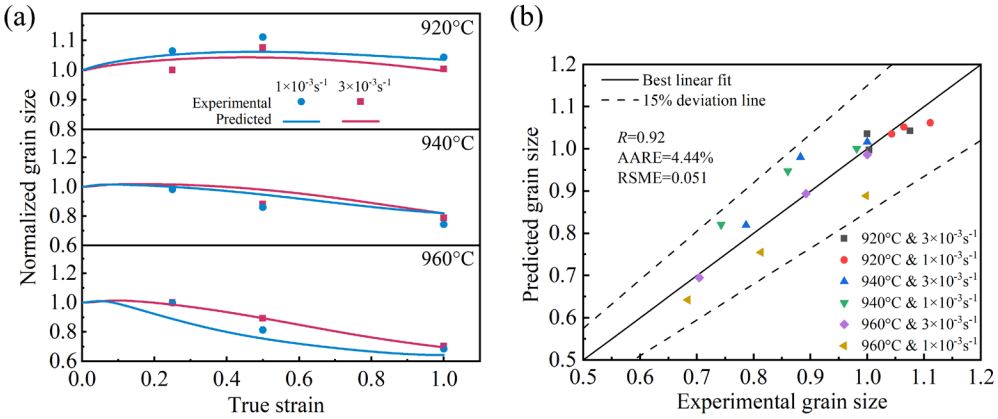

Fig. 6. (a) Comparison and (b) correlation between predicted normalized grain sizes (curves) of constitutive model and experimental results (points).

Conclusions

(1) The flow stress of TA32 alloy during superplastic deformation decreases as the temperature increases and strain rate decreases. Increasing temperature and strain rate promote the transformation of LAGBs to HAGBs, the disappearance of intragranular defects, α→β phase transformation, and the formation of more equiaxed grains. The microstructure of TA32 alloy varies little within the range of 1×10^{-3}-3×10^{-3} s^{-1}.

(2) Building upon the macroscopic and microscopic deformation characteristics of TA32 titanium alloy during superplastic deformation, a unified constitutive model is constructed, coupled with the grain size evolution. The model describes the interactions among physical variables such as flow stress, plastic strain rate, dislocation density, and average grain size and reflects the influence of microstructure on flow stress.

(3) The statistical results reveal the correlation coefficient *R*, AARE and RMSE between predicted and experimental stress values are 0.98, 6.91% and 1.94, respectively. Similarly, the correlation coefficient *R*, AARE and RMSE between predicted and experimental normalized grain size values are 0.92, 4.44% and 0.051, respectively. The unified constitutive model has a good prediction effect on the superplastic mechanic behavior and grain size evolution characteristics of TA32 alloy.

Acknowledgments

Authors acknowledge the funding supported by National Natural Science Foundation of China (No. U22A20186, 52211530441, 52175285) and Aeronautical Science Foundation of China (No. 2022Z047025001).

References

[1] S. Li, T.S. Deng, Y.H. Zhang, Y.Q. Liang, R.X. Li, T.H. Dong, Review on the creep resistance of high-temperature titanium alloy, Trans. Indian Inst. Met. 74 (2021) 215-222. https://doi.org/10.1007/s12666-020-02137-x

[2] C. Cheng, Y. Feng, Z.Y. Chen, H.E. Li, Q.J. Wang, X. Wang, Effect of annealing temperature on microstructure, texture and tensile properties of TA32 sheet, Mater. Sci. Eng. A 826 (2021) 141971. https://doi.org/10.1016/j.msea.2021.141971

[3] B. Babu, L.E. Lindgren, Dislocation density based model for plastic deformation and globularization of Ti-6Al-4V, Int. J. Plast. 50 (2013) 94-108. https://doi.org/10.1016/j.ijplas.2013.04.003

[4] Y.W. Xiao, Y.C. Lin, Y.Q. Jiang, X.Y. Zhang, G.D. Pang, D. Wang, K.C. Zhou, A dislocation density-based model and processing maps of Ti-55511 alloy with bimodal

microstructures during hot compression in α+β region, Mater. Sci. Eng., A 790 (2020) 139692. https://doi.org/10.1016/j.msea.2020.139692

[5] Q. Bai, J. Lin, T.A. Dean, D.S. Balint, T. Gao, Z. Zhang, Modelling of dominant softening mechanisms for Ti-6Al-4V in steady state hot forming conditions, Mater. Sci. Eng. A 559 (2013) 352-358. https://doi.org/10.1016/j.msea.2012.08.110

[6] T. Yasmeen, Z.T. Shao, L. Zhao, P. Gao, J. Lin, J. Jiang, Constitutive modeling for the simulation of the superplastic forming of TA15 titanium alloy, Int. J. Mech. Sci. 164 (2019) 105178. https://doi.org/10.1016/j.ijmecsci.2019.105178

[7] Y. Liu, Z.Q. Li, B. Zhao, T. Yang, C.Y. Sun, Superplastic deformation behavior and constitutive model of TA32 titanium alloy, Rare Metal Mat. Eng. 51 (2022) 3752-3761.

[8] J.W. Xu, W.D. Zeng, Q.Y. Zhao, D.D. Zhou, S.T. He, R.C. Jia, X.F. Zhou, Analysis of deformation behavior and microstructure of a near-alpha titanium alloy in single phase region, Mater. Sci. Eng. A 803 (2021) 140723. https://doi.org/10.1016/j.msea.2020.140723

[9] Y. Liu, Z.Q. Li, B. Zhao, C.y. Sun, Y.h. Feng, Microstructure evolution characteristics of near-α TA32 titanium alloy during superplastic tensile deformation, Mater. Sci. Eng., A 879 (2023) 145264. https://doi.org/10.1016/j.msea.2023.145264

[10] L. Despax, V. Vidal, D. Delagnes, M. Dehmas, H. Matsumoto, V. Velay, Influence of strain rate and temperature on the deformation mechanisms of a fine-grained Ti-6Al-4V alloy, Mater. Sci. Eng. A 790 (2020) 139718. https://doi.org/10.1016/j.msea.2020.139718

[11] J. Lin, T.A. Dean, Modelling of microstructure evolution in hot forming using unified constitutive equations, J. Mater. Process. Technol. 167 (2005) 354-362. https://doi.org/10.1016/j.jmatprotec.2005.06.026

[12] L. Yang, B.y. Wang, G. Liu, H.j. Zhao, J. Zhou, Hot tensile behavior and self-consistent constitutive modeling of TA15 titanium alloy sheets, J. Mater. Eng. Perform. 24 (2015) 4647-4655. https://doi.org/10.1007/s11665-015-1784-7

[13] J. Lin, M. Mohamed, D. Balint, T.A. Dean, The development of continuum damage mechanics-based theories for predicting forming limit diagrams for hot stamping applications, Int. J. Damage Mech. 23 (2013) 684-701. https://doi.org/10.1177/1056789513507731

[14] J. Lin, Y. Liu, D.C.J. Farrugia, M. Zhou, Development of dislocation-based unified material model for simulating microstructure evolution in multipass hot rolling, Philos. Mag. 85 (2005) 1967-1987. https://doi.org/10.1080/14786430412331305285

[15] J. Lin, Y. Liu, T.A. Dean, A review on damage mechanisms, models and calibration methods under various deformation conditions, Int. J. Damage Mech. 14 (2016) 299-319. https://doi.org/10.1177/1056789505050357

[16] E. Alabort, P. Kontis, D. Barba, K. Dragnevski, R.C. Reed, On the mechanisms of superplasticity in Ti-6Al-4V, Acta Mater. 105 (2016) 449-463. https://doi.org/10.1016/j.actamat.2015.12.003

[17] W. Roberts, B. Ahlblom, A nucleation criterion for dynamic recrystallization during hot working, Acta Mater. 26 (1978) 801-813. https://doi.org/10.1016/0001-6160(78)90030-5

[18] R. Sandström, R. Lagneborg, A model for hot working occurring by recrystallization, Acta Mater. 23 (1975) 387-398. https://doi.org/10.1016/0001-6160(75)90132-7

[19] J. Lin, A set of unified constitutive equations for modelling microstructure evolution in hot deformation, J. Mater. Process. Technol. 143-144 (2003) 281-285. https://doi.org/10.1016/s0924-0136(03)00472-2